

Measurement of the Electric and Magnetic Polarizabilities of the Proton

B. E. MacGibbon, G. Garino*, M. A. Lucas†, and A. M. Nathan
*Department of Physics, University of Illinois at Urbana-Champaign,
Urbana, Illinois 61801*

G. Feldman
*Saskatchewan Accelerator Laboratory, University of Saskatchewan,
Saskatoon, Saskatchewan Canada S7N 0W0*

B. Dolbilkin
*Institute for Nuclear Research, Russian Academy of Sciences
Moscow 117312 Russia*

(August 7, 2018)

Abstract

The Compton scattering cross section on the proton has been measured at laboratory angles of 90° and 135° using tagged photons in the energy range 70–100 MeV and simultaneously using untagged photons in the range 100–148 MeV. With the aid of dispersion relations, these cross sections were used to extract the electric and magnetic polarizabilities, $\bar{\alpha}$ and $\bar{\beta}$ respectively, of the proton. We find

$$\bar{\alpha} + \bar{\beta} = (15.0 \pm 2.9 \pm 1.1 \pm 0.4) \times 10^{-4} \text{ fm}^3,$$

in agreement with a model-independent dispersion sum rule, and

$$\bar{\alpha} - \bar{\beta} = (10.8 \pm 1.1 \pm 1.4 \pm 1.0) \times 10^{-4} \text{ fm}^3,$$

where the errors shown are statistical, systematic, and model-dependent, respectively. A comparison with previous experiments is given and global values for the polarizabilities are extracted.

13.60.Fz, 13.40.Fn., 14.20.Dh

I. INTRODUCTION

The electric and magnetic polarizabilities of the nucleon, labeled $\bar{\alpha}$ and $\bar{\beta}$ respectively, are fundamental structure constants that characterize the ability of the constituents of the nucleon to rearrange themselves in response to static or slowly varying external electric and magnetic fields. These parameters are as fundamental as the charge and magnetic radii of the nucleon, although they have received considerably less attention until fairly recently. With the high present-day interest in QCD-based descriptions of the structure of the nucleon, the additional information represented by an accurate determination of the polarizabilities would be of substantial importance. This question has motivated considerable activity in recent years on both theoretical and experimental fronts. In this Introduction, the experimental situation is reviewed; a discussion of the theoretical issues is presented in Section VI.

Measurements of the proton polarizabilities have come exclusively from Compton scattering experiments. These measurements rely on a theorem which establishes a unique relation between the model-independent low-energy expansion (LEX) of the Compton scattering cross section and the polarizabilities. For photon energies sufficiently low, this expansion in the laboratory frame reads [1]

$$\frac{d\sigma}{d\Omega}(\omega, \theta) = \frac{d\sigma^{\text{B}}}{d\Omega}(\omega, \theta) - \frac{e^2}{4\pi M} \left(\frac{\omega'}{\omega}\right)^2 (\omega\omega') \left\{ \frac{\bar{\alpha} + \bar{\beta}}{2}(1 + \cos\theta)^2 + \frac{\bar{\alpha} - \bar{\beta}}{2}(1 - \cos\theta)^2 \right\}, \quad (1)$$

where ω and ω' are the energies of the incident and scattered photons respectively, $e^2/4\pi$ is the fine structure constant, and $d\sigma^{\text{B}}/d\Omega$ is the exact Born cross section for a proton with an anomalous magnetic moment but no other structure [2]. The LEX is an expansion of the cross section to first order in $(\omega\omega')$; besides the anomalous magnetic moment, the only structure-dependent terms to this order are the polarizabilities. The equation shows that the forward and backward cross sections are sensitive mainly to $\bar{\alpha} + \bar{\beta}$ and $\bar{\alpha} - \bar{\beta}$, respectively, whereas the 90° cross section is sensitive only to $\bar{\alpha}$. The sum $\bar{\alpha} + \bar{\beta}$ is independently constrained by a model-independent dispersion sum rule [3]:

$$\bar{\alpha} + \bar{\beta} = \frac{1}{2\pi^2} \int_{m_\pi}^{\infty} \frac{\sigma_\gamma(\omega) d\omega}{\omega^2} = 14.2 \pm 0.5, \quad (2)$$

in units of 10^{-4} fm^3 (these units are implicitly understood hereafter), where $\sigma_\gamma(\omega)$ is the total photoabsorption cross section on the proton. The numerical value in Eq. 2 is obtained using both the available experimental data and a reasonable theoretical *ansatz* for extrapolating the integral to infinite energy [4,5].

The polarizabilities are determined by measuring the deviation of the cross sections from the Born values. A plot of the Born and LEX cross sections is shown in Fig. 1. The curves show that the effect of the polarizabilities, which is proportional to the difference between the Born and LEX curves, is not very large, thereby placing great demand on the statistical precision and systematic accuracy of the measurements in order to obtain precise values for the polarizabilities. Those demands can be relaxed by going to a higher photon energy, since the sensitivity of the cross section to the polarizabilities increases with energy. However if the energy becomes too large, the LEX breaks down and theoretical uncertainty is introduced into the extraction of the polarizabilities from the measured cross sections. This is demonstrated in Fig. 1, where the curve labeled DR is a calculation of the cross section using dispersion relations and is valid, in principle, at all energies. This curve shows that the LEX is not valid above about 100 MeV. Since many of the experiments, including the present measurements, have been done at energies outside the range of validity of the LEX, it is necessary to pay particular attention to the model dependence in the determination of the polarizabilities from the cross sections. This issue is discussed at length in Section IV.

The above considerations suggest that the experimental challenge for determining the proton polarizabilities is to measure an *absolute* cross section over an energy and angular range that is appropriately balanced between sensitivity to the polarizabilities and insensitivity to any theoretical model. With this in mind, it is useful to examine briefly the previous experiments that have attempted to determine the proton polarizabilities from measurements of the Compton scattering cross section [6–10], some of which are summarized in Table I.

The pioneering experiment is that of Gol'danski [6], whose original result ($\bar{\alpha} = 9 \pm 2$) is omitted from the list mainly because the 8% uncertainty in the normalization of the cross sections leads to a systematic uncertainty in $\bar{\alpha}$ of ± 5 [11]. Also omitted is an earlier Compton scattering experiment [12] with energies, angles, and systematic errors comparable to those of Gol'danski, although no attempt was made by the author to extract polarizabilities from the cross sections. In both cases the systematic uncertainty on the polarizabilities is too large to affect the global fit we will report in Section V.

The Moscow 1975 experiment [7] used a bremsstrahlung photon beam and a photon detector with very poor energy resolution. Nevertheless, due to a clever technique that allowed the cross section to be normalized to the well-known Klein-Nishina cross section for Compton scattering on the electron, the systematic errors were thought to be small. The reported polarizabilities were based on a fit to the cross sections using the LEX. Since the maximum energy of those cross sections (110 MeV) is outside the range of validity of the LEX, we have refitted them using the dispersion-relation technique described in Section V, and those results are given in Table I. Unfortunately they are badly inconsistent with the dispersion sum rule, thereby casting doubt on the cross sections and providing the principal motivation for the more recent experiments.

The Illinois 1991 experiment [8] had two very desirable features. First, it was done at both a forward and backward scattering angle and at low energies, so that model-independent determinations of both $\bar{\alpha} + \bar{\beta}$ (testing the dispersion sum rule and/or the systematics of the experiment) and $\bar{\alpha} - \bar{\beta}$ were possible. Second, a tagged photon beam was used, thereby considerably improving the ability to measure absolute cross sections accurately. Unfortunately, the combined effects of low energy (implying low sensitivity) and the counting rate limitations inherent in a tagged photon experiment resulted in reduced statistical precision in the extracted polarizabilities.

The Mainz 1992 experiment [9] measured the 180° Compton cross section by detecting the recoil proton at 0° in a magnetic spectrometer, normalizing to the Compton cross section on the electron. The energy, 132 MeV, was a good compromise between sensitivity to the

polarizabilities and model independence. The principal drawback of this experiment was that $\bar{\alpha} - \bar{\beta}$ was determined by just a single cross-section measurement at one energy and angle.¹

The Saskatoon 1993 experiment [10] used a high duty-factor bremsstrahlung photon beam and a high-resolution NaI detector to measure an extensive set of angular distributions via the endpoint technique. While the statistical and systematic quality of the data were very good, the energies (150–300 MeV) were far outside the range of validity of the LEX, leading to possibly large uncertainties in the polarizabilities due to model-dependent effects.

We report here new measurements of the Compton scattering cross sections and the extraction of improved values for the electric and magnetic polarizabilities from those cross sections. The measurements utilized a new experimental technique, described in Sections II and III, in which measurements were done simultaneously using tagged photons (70–100 MeV) and untagged photons (100–148 MeV). An important feature of this work is a careful consideration of the model dependence in the extraction of the polarizabilities from the cross sections; the theoretical background for this discussion is presented in Section IV. In Section V, the actual procedure used to extract the polarizabilities is presented, and the new values derived from both the present experiment and a global fit to all the recent experiments are given. A brief discussion of the theoretical impact of the results is given in Section VI and our conclusions are summarized in Section VII. An extensive account of this work can be found in the Ph.D. dissertation of MacGibbon [13].

II. EXPERIMENT

The Compton scattering cross section for the proton was measured at the Saskatchewan Accelerator Laboratory (SAL) using tagged photons with energies from 70 to 100 MeV

¹Actually cross sections were measured at both 132 and 98 MeV, but the the latter datum has poor statistical quality and does not provide a serious constraint on the polarizabilities.

and untagged photons with energies from 100 to 148 MeV. The entire energy region 70–148 MeV was measured simultaneously. A high duty-factor ($\sim 70\%$) beam of 148-MeV electrons was incident on a 115- μm aluminum radiator, creating a continuous bremsstrahlung spectrum of photons up to the endpoint. The electron beam energy was chosen to minimize the background from the π^0 -decay photons. The photon beam was collimated so that its diameter was ~ 6 cm at the target position. Approximately 25% of the photon beam was removed by the collimation. The primary electron beam was bent away from the photon beam by the main tagging magnet and steered into a shielded beam dump by a secondary magnet.

The SAL tagger [14] was used to determine the energy of the tagged photons by momentum analyzing the associated electrons in the tagging magnet and detecting them in a 62-channel scintillator hodoscope in coincidence with the scattered photons. With the electron beam energy of 148 MeV, the magnetic field was set to tag 70–100 MeV photons with an average resolution of ~ 0.5 MeV for each of the 62 channels. The total tagged photon flux, integrated over the 62 channels, was approximately $7 \times 10^7 \text{ sec}^{-1}$.

The scattering target was liquid hydrogen. The target assembly was a closed-loop recirculation system consisting of a two-stage refrigerator, a target flask and reservoir, and transfer tubes. The 0.25-mm thick Mylar target flask was a cylinder 10.16 cm in diameter and ~ 13 cm long, oriented with the symmetry axis along the beam direction. After the initial cooldown and liquification, the flask could be remotely emptied or filled in ~ 20 minutes, thereby facilitating the process of alternating between full-target and empty-target runs. The flask was contained in an aluminum vacuum chamber; the detectors were shielded from the photons scattered from the 0.25 mm Mylar windows isolating the vacuum chamber from the atmosphere.

By measuring the transmission of photons through the target, its thickness was determined *in situ*. A tightly collimated beam of 0.661-MeV photons from a ^{137}Cs source was used. By counting the number of photons transmitted by both the full and empty target and by using the known mass absorption coefficient of hydrogen [15], the target thickness

was determined to be 13.00 ± 0.15 cm, or $(5.43 \pm 0.06) \times 10^{23}$ protons/cm², in agreement with the geometrical measurement.

The photons were detected in two large-volume high-resolution NaI(Tl) spectrometers, one each at scattering angles of 90° and 135° and each subtending a geometrical solid angle of ~ 0.05 sr. The NaI crystals were surrounded by plastic anti-coincidence shields to reject cosmic rays and other charged particles and by 10.2 cm-thick Pb shields to reduce the effects of room background.

The gains of the detectors were monitored during data acquisition and corrected for drifts over the course of the three-week run. An LED was mounted on the back of each NaI detector together with an annular silicon surface-barrier detector (SBD), so that both the SBD and the NaI were illuminated by photons from the LED. The LED was flashed at two different intensities, allowing a monitor of both the gain and offset of each photomultiplier tube (PMT) and its associated electronics. The SBD, which was used to monitor and correct the intensity of the LED pulses, was determined to be stable to better than 0.5% in bench tests with an α -particle source. The corrected gain of each NaI was stable to better than 0.4% throughout the course of the experiment.

The overall trigger for the experiment was a signal with an energy above threshold in either of the two NaI detectors. All such events were accepted whether or not they were accompanied by a tagging electron, thereby allowing the acquisition of both tagged and untagged events simultaneously. For each event, the ADC value for each of the NaI PMT's was recorded along with the 62 TDC values corresponding to the time difference between a NaI signal and each of the tagging electrons. At 15-second intervals, the 62 scalers counting the number of electrons in each tagging channel were read out. The data were sorted off-line into tagged and untagged events. A tagged event was defined as one in which the photon was correlated with a tagging electron, and an untagged event was defined as *any* photon event. Thus, the tagged events were a *subset* of the untagged events.

Data were collected by alternating between full-target runs of ~ 6 hours and empty-target runs of ~ 4 hours. At three different times during the experiment, each NaI detector

was placed directly in the photon beam in order to measure the ratio of the number of photons incident on the target to the number of tagging electrons (the so-called tagging efficiency) and to determine the detector response functions (see Section III) and energy calibration. A Pb-glass detector was also periodically placed in the photon beam in order to provide a relative monitor of the tagging efficiency, which was determined to be stable to better than $\pm 0.5\%$ throughout the course of the experiment.

III. DATA REDUCTION

Since the present technique of simultaneous measurements with tagged and untagged photons is new, it is discussed here in some detail. The technique is shown schematically in Fig. 2 and consists of two types of measurements: (1) a scattering run, which measures the detector pulse-height spectrum for scattered photons normalized to the number of electrons n_e detected in the tagger; and (2) a calibration run which is used to normalize n_e to the number of photons incident on the target. The latter is accomplished by putting the detector directly into the photon beam. Together these measurements are used to determine the scattering cross section.

For both the tagged and untagged data, the scattering cross sections were determined from the detector pulse-height spectrum of scattered photons:

$$\frac{dN_s(E)}{dE} = \int_0^{E_0} \frac{dN_i(E_\gamma)}{dE_\gamma} \kappa \Omega \frac{d\sigma(E_\gamma)}{d\Omega} \frac{dR_s(E_\gamma, E)}{dE} dE_\gamma, \quad (3)$$

where κ is the target thickness, Ω is the detector solid angle, E_γ is the incident photon energy, E is the pulse height in the detector, and E_0 is the endpoint energy. This expression is the convolution of the bremsstrahlung photon spectrum incident on the target $dN_i(E_\gamma)/dE_\gamma$, the scattering cross section $d\sigma(E_\gamma)/d\Omega$, and the detector response function for scattered photons $dR_s(E_\gamma, E)/dE$. This latter quantity is the probability density that a photon of energy E_γ incident on the front face of the NaI detector will register a pulse height E in

that detector.² The detector pulse-height spectrum in a calibration run is used to measure the incident photon flux:

$$\frac{dN_c(E)}{dE} = \int_0^{E_0} \frac{dN_i(E_\gamma)}{dE_\gamma} \frac{dR_c(E_\gamma, E)}{dE} dE_\gamma, \quad (4)$$

where the detector response function in the calibration run $dR_c(E_\gamma, E)/dE$ differs slightly from that in the scattering run $dR_s(E_\gamma, E)/dE$ due to the different geometries and the Compton recoil shift.

A. Tagged Photon Analysis

For the tagged-photon measurements, each incident tagged-photon energy bin is a 0.5-MeV slice of the full bremsstrahlung spectrum, or essentially a δ -function:

$$\frac{dN_i(E_\gamma)}{dE_\gamma} \approx n_t(E_t) \delta(E_\gamma - E_t), \quad (5)$$

where E_t is the tagged-photon energy and n_t is the number of tagged photons in that bin. Therefore the pulse-height spectrum for a calibration run is given by

$$\frac{dN_c(E)}{dE} = n_{ec} \epsilon_t \frac{dR_c(E_t, E)}{dE}, \quad (6)$$

where n_{ec} is the number of associated tagging electrons measured with the tagger scalers, and $\epsilon_t \equiv n_t(E_t)/n_{ec}$ is the tagging efficiency. This latter quantity is determined experimentally by taking the ratio of the total number of counts in the pulse-height spectrum to n_{ec} . Note that the tagged-photon pulse-height spectrum is a direct measure of the shape of the detector response function in the calibration mode. A typical spectrum is shown in Fig. 3 which also shows a Monte Carlo simulation of the response function using the code EGS4

²Strictly speaking, the first argument of the scattering response function should be E'_γ , the scattered photon energy, which differs from the incident energy due to the Compton recoil shift. For simplicity of notation, this recoil shift has been absorbed into the response function.

[16]. The excellent agreement between the calculated and measured response functions for the calibration geometry gives us confidence that EGS4 can be used to calculate the detector response for the scattering geometry, where it is not so easily measured. Previous experience with the same detectors at similar photon energies has shown that EGS4 *can* accurately account for scattering line shapes in experiments where they can be measured with good statistics [17].

Again using Eq. 5, the detector pulse-height spectrum for tagged photons in a scattering run is related to the cross section by

$$\frac{dN_s(E)}{dE} = n_{\text{es}} \epsilon_t \kappa \Omega \frac{d\sigma}{d\Omega}(E_t) \frac{dR_s(E_t, E)}{dE}, \quad (7)$$

where n_{es} is the number of tagging electrons measured with the tagger scalers, and the value of ϵ_t is obtained from the calibration run. The detector response function is again determined using an EGS4 simulation, which now also accounts for the effects of the finite geometry on κ and Ω , as well as the Compton recoil shift. For each tagger channel, cuts are placed on the TDC value (see Fig. 4) to obtain separate true-plus-random and random pulse-height spectra. The appropriately normalized random spectrum, which is corrected for rate-dependent losses in the TDC, is then subtracted from the true-plus-random one to obtain a true coincidence spectrum, which is then shifted to a common energy and combined with those of adjacent tagger channels into one of four composite spectra, each corresponding to a tagging range of about 8 MeV. This is done separately for the full-target and empty-target data, which are then subtracted to obtain final spectra for scattering from hydrogen.³ These spectra are then integrated to obtain $d\sigma/d\Omega$. A sample hydrogen scattering spectrum together with a normalized EGS4 spectrum is shown in Fig. 5. The resulting tagged-photon cross sections are given in the Appendix.

³A 2% correction is made for the residual gas in the target flask during the empty-target runs.

B. Untagged Photon Analysis

The untagged cross sections were also determined using Eqs. 3 and 4. To simplify the notation, the incident photon spectrum is expressed as

$$\begin{aligned}\frac{dN_i(E_\gamma)}{dE_\gamma} &= n_0 f(E_\gamma) \\ &= n_{ec} \epsilon_u f(E_\gamma),\end{aligned}\tag{8}$$

where n_0 is the total number of incident photons with energy in the interval between $E_1=100$ MeV and the endpoint energy E_0 , $f(E_\gamma)$ is the spectrum shape that is normalized to unit area over the same energy interval, and ϵ_u is the ratio of n_0 to the number of electrons measured by the tagger scalars. Thus for the untagged analysis, the tagger is only used to normalize the number of photons in a calibration run to that in a scattering run. The pulse-height spectrum in a calibration run (see Eq. 4) now takes the form

$$\frac{dN_c(E)}{dE} = n_{ec}\epsilon_u \int_{E_1}^{E_0} f(E_\gamma) \frac{dR_c(E_\gamma, E)}{dE} dE_\gamma.\tag{9}$$

The quantity ϵ_u is determined by normalizing the calibration pulse-height spectrum to a calculated spectrum. In the calculation, the detector response function is again determined using EGS4,⁴ and the shape $f(E_\gamma)$ is taken to be the Schiff bremsstrahlung spectrum [18], which is differential in both energy and angle. The resulting normalized spectrum for one of the detectors is shown in Fig. 6 along with the data. It was verified that the cross sections derived from this technique are insensitive to the exact form of $f(E_\gamma)$.

The cross sections are found by fitting the scattering pulse-height spectrum to the expression (see Eq. 3):

⁴For the untagged analysis, it was necessary to have detector response functions up to 148 MeV. Since the maximum tagged photon energy in the setup was 100 MeV, a supplemental experiment was performed *in situ* with higher-energy electrons in order to measure the detector response. It was verified that the EGS4 simulation continues to describe the measured response function up to an energy of 148 MeV.

$$\frac{dN_s(E)}{dE} = n_{es}\epsilon_u \int_{E_1}^{E_0} f(E_\gamma) \kappa\Omega \frac{d\sigma}{d\Omega}(E_\gamma) \frac{dR_s(E_\gamma, E)}{dE} dE_\gamma, \quad (10)$$

using a simple parametrization of the cross section:

$$\frac{d\sigma}{d\Omega}(E_\gamma) = \begin{cases} S_1 & \text{for } E_\gamma = 100\text{--}110 \text{ MeV} \\ S_2 & \text{for } E_\gamma = 110\text{--}120 \text{ MeV} \\ S_3 & \text{for } E_\gamma = 120\text{--}130 \text{ MeV} \\ S_4 & \text{for } E_\gamma = 130\text{--}140 \text{ MeV} \\ S_5 & \text{for } E_\gamma = 140\text{--}150 \text{ MeV.} \end{cases} \quad (11)$$

The S_i were allowed to vary freely to obtain the best fit to the final scattering spectrum (with empty-target subtracted) over the energy range corresponding to incident photons between 100 MeV and the endpoint energy. These parameters have a high degree of anti-correlation between adjacent values due to the low-energy tail on the detector response function; therefore it was necessary to employ the full error matrix when using these cross sections to extract physical quantities. The scattering spectra and the associated fits are shown in Fig. 7. The resulting untagged cross sections and associated errors are given in the Appendix.

It is noted that since the tagged data are a subset of the untagged data, the minimum incident energy for which untagged results are quoted (100 MeV) is the maximum energy for which we have tagged results. Thus the same photon event is not counted as both tagged and untagged. However, as a check of our technique, we investigated the overall consistency between the tagged and untagged cross sections by extending the calculation shown in Fig. 7 into the tagging region using the tagged cross sections given in the Appendix. At 135° there is good consistency. However, at 90° the curve is consistently below the data, indicating that those data are contaminated with non-Compton events from the target, such as π^0 -decay photons, whose kinematic endpoint is just below the maximum tagging energy of 100 MeV, or pair production followed by bremsstrahlung. This is not a problem for energies above the tagging region.

C. Systematic Errors

The overall systematic uncertainty for the cross sections is $\pm 2.9\%$ for the untagged data and ranges from $\pm 3.0\%$ to $\pm 4.0\%$ for the tagged data. Typical contributions include the uncertainties in the detector solid angle ($\pm 1.2\%$), target thickness ($\pm 1.2\%$), tagging efficiency ($\pm 1-2\%$), and rate-dependent corrections ($\pm 1-3\%$). A complete discussion of these errors and the details of the experimental procedure and data reduction have been given by MacGibbon [13]. It should be noted that the different systematic errors had various degrees of correlation among the different cross sections (e.g., the error due to the target thickness was correlated among all the cross sections, while that due to the solid angle of the 135° detector was correlated only among the 135° cross sections). The effect of these correlations was properly taken into account when extracting the polarizabilities.

IV. THEORETICAL CONSIDERATIONS

Since much of the data in the current experiment lie outside the range of validity of the LEX, it is necessary to address the issue of how to extract the polarizabilities from the cross sections and the model dependence therein. In this section, a theoretical overview of the dispersion-relation approach utilized here is presented. This approach, as well as the computer code used for the numerical work, are due to L'vov [19]. A more complete description will be published elsewhere [20].

All Compton scattering observables are determined from six independent invariant amplitudes, $A_i(\nu, t)$, which are free of kinematical singularities and constraints and are even functions of $\nu = (s - u)/4M$. Here s , t , and u are the usual Mandelstam variables and M is the proton mass. These amplitudes incorporate different mechanisms for Compton scattering, including s -, u -, and t -channel exchanges of stable particles (see diagrams in Fig. 8). The s - and u -channel processes are sums over all possible intermediate states that can be formed in the photon-proton interaction, such as nucleon resonances, non-resonant

π -nucleon states, etc. For the special case where the intermediate state is a proton in the ground state, the so-called Born amplitude, A_i^B , is obtained. This purely real amplitude is calculated exactly in terms of the charge, mass, and magnetic moment of the proton; the cross section based on the A_i^B alone is shown in Fig. 1. All other diagrams, including the t -channel exchanges, contribute to the non-Born part, A_i^{NB} . At low energies, the Born and non-Born parts combine to give the LEX, with the polarizabilities identified as:

$$\begin{aligned}\bar{\alpha} + \bar{\beta} &= -\left(\frac{1}{2\pi}\right) [A_6^{\text{NB}}(0,0) + A_3^{\text{NB}}(0,0)] \\ \bar{\alpha} - \bar{\beta} &= -\left(\frac{1}{2\pi}\right) A_1^{\text{NB}}(0,0).\end{aligned}\tag{12}$$

If A_i falls sufficiently rapidly with increasing energy, it satisfies an unsubtracted fixed- t dispersion relation:

$$\text{Re}[A_i(\nu, t)] = A_i^B(\nu, t) + \frac{2}{\pi} \mathcal{P} \int_{\nu_0}^{\infty} \frac{\nu' \text{Im}[A_i(\nu', t)]}{\nu'^2 - \nu^2} d\nu',\tag{13}$$

where ν_0 is the threshold for pion photoproduction. The imaginary parts of the scattering amplitudes are related to the multipole amplitudes for the total photoabsorption cross section on the proton through unitarity. Therefore, provided the dispersion relations are valid, a complete knowledge of the multipole amplitudes at all energies uniquely determines the scattering cross section and therefore the polarizabilities. However for some of the amplitudes an unsubtracted dispersion relation is *not valid* because the integral does not converge. This is largely due to the t -channel processes (see Fig. 8), which give rise to amplitudes that do not fall rapidly enough with energy to assure convergence of the integral. Indeed, the t -channel exchange of a stable particle such as a π^0 leads to an amplitude which is independent of ν and unconstrained by the multipole amplitudes (see Eq. 17). For such amplitudes, Eq. 13 is not valid and consequently the scattering cross section is not uniquely determined by the photoabsorption cross section.

Different approaches have been used to handle the convergence problem [19,21,22]. The approach utilized by L'vov [19] is to terminate the integral at $\nu_m = 1.5$ GeV and close the contour with a semicircle \mathcal{C} of radius ν_m in the upper half of the complex ν -plane. The

dispersion relation then takes the form

$$\text{Re} [A_i(\nu, t)] = A_i^{\text{B}}(\nu, t) + A_i^{\text{int}}(\nu, t) + A_i^{\text{asympt}}(\nu, t), \quad (14)$$

where the integral part A_i^{int} is given by

$$A_i^{\text{int}}(\nu, t) = \frac{2}{\pi} \mathcal{P} \int_{\nu_0}^{\nu_m} \frac{\nu' \text{Im} [A_i(\nu', t)]}{\nu'^2 - \nu^2} d\nu', \quad (15)$$

and the asymptotic part A_i^{asympt} is given by

$$A_i^{\text{asympt}}(\nu, t) = \text{Im} \left[\frac{1}{\pi} \int_{\mathcal{C}} \frac{\nu' A_i(\nu', t)}{\nu'^2 - \nu^2} d\nu' \right]. \quad (16)$$

It should be emphasized that this procedure is exact and does not rely on any special assumptions about the behavior of the amplitudes at very large energies. It expresses the real part of the invariant amplitude as a sum of a Born part which is calculated exactly, an integral part which is determined by the photoabsorption multipole amplitudes, and an asymptotic part. The integral and asymptotic contributions are now discussed separately.

The integral part is discussed first. As mentioned above, unitarity relates $\text{Im}[A_i]$ to the multipole amplitudes for the total photoabsorption cross section on the proton. For Compton scattering near and below the pion threshold, the most important intermediate states contributing to the dispersion integrals are the πN states (including nucleon resonances that decay into the πN channel), which have both the largest cross section and the largest energy weighting. For this contribution, $\text{Im}[A_i]$ is a sum of bilinear combinations of single-pion photoproduction multipole amplitudes, the most important of which have been very well measured and tabulated [23,24]. Thus the πN contribution to the dispersion integrals can be reliably calculated, and the sensitivity of the scattering cross section to experimental uncertainties in the πN multipoles can be readily determined. On the other hand, the multipole amplitudes for multi-pion photoproduction, which dominates the photoabsorption cross section for energies greater than ~ 600 MeV, are poorly known experimentally and therefore can only be treated in the context of a model. Fortunately, for photon scattering energies below 150 MeV, the multi-pion contribution to the dispersion integrals is

suppressed because of the large energy denominator, so it is expected that the predicted scattering cross sections will only weakly depend on the model assumptions. Approximately 40% of the multi-pion cross section proceeds either through known resonances or through the ρN channel, and these contributions can be reliably decomposed into multipoles. The non-resonant cross section is partly due to $\pi\Delta$ production. For partial waves $l \geq 1$, the multipole amplitudes for this process are calculated in the Born approximation, assuming a one-pion-exchange mechanism. The remaining multi-pion cross section, hereafter referred to as the non-resonant s-wave contribution, is ascribed some combination of low-order multipoles, leading to non-resonant intermediate states with $j^\pi = 1/2^+, 1/2^-,$ or $3/2^-$, and then scaled so that the calculated total multi-pion contribution to the photoabsorption reproduces the experimental value at each energy. The sensitivity of the scattering cross section to the model can be tested by adjusting the combination of multipoles making up the non-resonant s-wave contribution.

The asymptotic part is discussed next. Using Regge theory, L'vov shows [19] that for $i=3-5$, $A_i(\nu, t)$ drops sufficiently rapidly at high ν and fixed t to assure negligible contribution of A_i^{asympt} for $\nu_m = 1.5$ GeV. However, both A_1 and A_2 and to a lesser extent A_6 have important contributions due to t -channel exchanges, so that the asymptotic part cannot be neglected. For $\nu \ll \nu_m$, the asymptotic amplitude due to the t -channel exchange of a particle x is ν -independent and has the general form (see Fig. 8)

$$A_i^{\text{asympt}}(t) = -\frac{g_{xNN}f_{x\gamma\gamma}}{t - m_x^2} F(t - m_x^2), \quad (17)$$

where g_{xNN} and $f_{x\gamma\gamma}$ are the $N \rightarrow Nx$ and $x \rightarrow \gamma\gamma$ coupling constants respectively, F is the product of vertex form factors, and m_x is the mass of the exchanged particle. This leads to a ν -independent amplitude whose t -dependence is mainly determined by m_x^2 . In reality there may be a whole family of exchanged particles, leading to a more complicated t -dependence. Nevertheless, for the low t of the scattering data considered here ($|t| \leq 0.06$ GeV²), the amplitude is completely dominated by the lowest-mass exchanged particle, and the effect of higher-mass exchanges can be absorbed into the form factor F .

For A_2 the lowest-mass exchanged particle is a π^0 , for which the coupling constants are known experimentally to within approximately $\pm 4\%$ [25,26]. The vertex form factor is of the form $F = e^{B_\pi(t-m_\pi^2)}$, with B_π in the range 0–3 GeV^{-2} [20,26]. Therefore, up to uncertainties in the coupling constants and the form factor, A_2^{asympt} can be calculated, and the effect of the uncertainties on the scattering cross sections can be tested.

For A_1 the leading exchange is that due to a correlated pair of pions in a 0^+ isoscalar state, for which the mass and the couplings are poorly known. For low t , it is convenient to express A_1^{asympt} in the alternate form

$$A_1^{\text{asympt}}(t) = C_{2\pi} e^{B_{2\pi} t/2}, \quad (18)$$

where $B_{2\pi} \approx 2/m_{2\pi}^2$ and $C_{2\pi} = -g_{(2\pi)NN} f_{(2\pi)\gamma\gamma}/m_{2\pi}^2$. The parameter $B_{2\pi}$ can be estimated either from the systematics of the t -dependence of Compton scattering in the vicinity of $E = 1.5$ GeV, from which $B_{2\pi} \approx 6$ GeV^{-2} [27], or from the Regge parametrization of pp -scattering polarization data, from which $B_{2\pi} \approx 10$ GeV^{-2} [19,28]. This range for $B_{2\pi}$ (6–10 GeV^{-2}) corresponds to $m_{2\pi}$ in the range 447–577 MeV, in agreement with expectations based on phenomenological descriptions of the NN interaction [29]. It is also consistent with the t -dependence calculated via a backward dispersion relation, using the physical amplitudes for the process $\gamma\gamma \rightarrow \pi\pi \rightarrow N\bar{N}$ [20]. Once again, the sensitivity of the scattering cross sections to the value of $B_{2\pi}$ can be tested. The remaining constant $C_{2\pi}$ is related to the difference of the polarizabilities, as can be seen by combining and rearranging Eqs. 12, 14, 15, and 18:

$$\bar{\alpha} - \bar{\beta} = - \left(\frac{1}{\pi^2} \right) \left\{ \int_{\nu_0}^{\nu_m} \text{Im} [A_1(\nu, 0)] \frac{d\nu}{\nu} + \frac{\pi C_{2\pi}}{2} \right\}. \quad (19)$$

In the analysis described below, $C_{2\pi}$ is treated as a free parameter which is adjusted to fit the scattering cross sections. This is equivalent to treating $\bar{\alpha} - \bar{\beta}$ as a free parameter.

For A_6 , it follows from Regge theory that the unsubtracted dispersion relation, Eq. 13, actually converges [19], although it is also known experimentally that the integral is not saturated by 1.5 GeV [30]. For $\nu \ll \nu_m$, A_6^{asympt} is approximately ν -independent and has a t -dependence of the form [19,31]

$$A_6^{\text{asympt}}(t) = C_P e^{B_P t/2}, \quad (20)$$

with B_P in the range 6–10 GeV⁻² [27,31]. The remaining constant C_P is related to the sum of polarizabilities by

$$\bar{\alpha} + \bar{\beta} = \frac{1}{2\pi^2} \int_{\omega_0}^{\omega_m} \frac{\sigma_\gamma(\omega)}{\omega^2} d\omega - \frac{C_P}{2\pi}. \quad (21)$$

By comparing the above equation with the sum rule (see Eq. 2), it is seen that the term involving C_P represents that part of the sum rule that is missing when the integral is terminated at $\omega_m=1.5$ GeV; numerically, it has the value $C_P/2\pi \approx -0.9$. The possibility that the experimental value of $\bar{\alpha} + \bar{\beta}$ is different from the sum-rule value can be investigated by treating C_P as a free parameter that is adjusted to fit the scattering data.

In summary, fixed- t dispersion relations can be used to predict the Compton scattering cross section below about 150 MeV in terms of two parameters, $C_{2\pi}$ and C_P (or equivalently $\bar{\alpha} - \bar{\beta}$ and $\bar{\alpha} + \bar{\beta}$), which are then adjusted to fit the scattering data. The calculations rely on the experimentally known single-pion photoproduction multipole amplitudes [23,24], a model for the multi-pion photoproduction multipole amplitudes, and certain assumptions about the asymptotic behavior. Specifically, it is assumed that A_{3-5}^{asympt} are negligible, that A_2^{asympt} is dominated by π^0 exchange, and that the *ansatz* of Eqs. 18 and 20 are valid for A_1^{asympt} and A_6^{asympt} , respectively. The principal sources of uncertainty are as follows:

- uncertainties in the single-pion multipole amplitudes for A_i^{int}
- model uncertainties in the calculation of the multi-pion multipole amplitudes for A_i^{int}
- experimental uncertainties in the π^0 -exchange couplings for A_2^{asympt}
- theoretical uncertainty in B_π , which modulates the t -dependence of A_2^{asympt}
- theoretical uncertainty in $B_{2\pi}$, which governs the t -dependence of A_1^{asympt}
- theoretical uncertainty in B_P , which governs the t -dependence of A_6^{asympt}

The sensitivity of the value extracted for $\bar{\alpha} - \bar{\beta}$ to these aspects of the dispersion calculation will be discussed in the next section. The numerical work was done using variations of the computer code GNGN, which was written and supplied by L'vov.

V. DETERMINATION OF THE POLARIZABILITIES

A. Fitting Procedure

The polarizabilities were determined by fitting the theoretical curves to the experimental cross sections, taking full account of the statistical and systematic errors. As remarked above, the statistical errors for the five individual untagged cross sections for each angle are correlated, thereby necessitating the use of the full 5×5 error matrix. The inclusion of the systematic errors in the fit is important since a 1% change in the overall normalization of every cross section results in a change in the extracted value of $\bar{\alpha} - \bar{\beta}$ by approximately 0.5. To determine the effect of the systematic errors on the polarizabilities, it is assumed that they are mainly errors of normalization in the measured cross sections. A standard technique is used to account for the systematic errors from different independent data sets [32]. For each data set, χ^2 is defined as follows:

$$\chi^2 = \left(\frac{\sigma^{\text{th}} - N\sigma^{\text{exp}}}{N\epsilon} \right)^2 + \left(\frac{N-1}{\epsilon_N} \right)^2, \quad (22)$$

where σ^{exp} and ϵ are the experimental scattering cross section and statistical error, respectively, and σ^{th} is the corresponding calculated scattering cross section. The second term of Eq. 22 takes into account the contribution of the normalization to χ^2 , where N is the normalization constant and ϵ_N is the systematic error. The total value of χ^2 is obtained by summing the χ^2 for each data set. Fits could be subjected to the sum-rule constraint by including an additional data set consisting of a single datum, whose experimental value and uncertainty are 14.2 ± 0.5 (see Eq. 2) and whose corresponding calculated value is equal to $\bar{\alpha} + \bar{\beta}$. Standard least-squares fitting procedures were used to adjust $\bar{\alpha}$, $\bar{\beta}$, and the normalization constants in order to minimize the total χ^2 . The net result is that each data set is

properly weighted based on its systematic error, taking full account of the correlations in those systematic errors, and the uncertainties in the fitted parameters (i.e., the polarizabilities) include contributions from both the statistical and the systematic errors. The purely statistical contribution to those uncertainties can be determined by fitting with fixed values for the normalization constants. The net systematic contribution is derived by assuming the total uncertainty is the result of combining in quadrature the statistical and systematic contributions. A detailed discussion of this technique is given by MacGibbon [13].

B. Present Experiment

Fits were done using cross sections calculated with the fixed- t dispersion relations, treating $\bar{\alpha} + \bar{\beta}$ and $\bar{\alpha} - \bar{\beta}$ as free parameters. In addition, the sensitivity of the results derived for $\bar{\alpha}$ and $\bar{\beta}$ to the uncertainties in the calculation was investigated. The results of this investigation are presented in Table II and a typical fit to the scattering cross sections is shown in Fig. 9. The sensitivity to the πN multipole amplitudes was studied by doing fits with each of four available tabulations of those amplitudes. One was the Metcalf-Walker 1975 tabulation [23]; the remaining three were from the more recent VPI tabulations [24], specifically the SP92, FA93, and SP95 data sets. The sensitivity to the model assumptions in the calculation of the multi-pion multipole amplitudes was studied by adjusting the multipole composition of the non-resonant s-wave contribution. The sensitivity to the product of coupling constants for the π^0 exchange amplitude ($g_{\pi NN} f_{\pi\gamma\gamma}$) was studied by varying the product within the range of its experimental uncertainty, $\pm 4\%$. Finally, the sensitivity to each of the three parameters describing the t -dependence of the asymptotic amplitudes was studied by varying them within the ranges $B_{\pi=0-3}$, $B_{2\pi=6-10}$, and $B_{P=6-10}$ GeV⁻².

Each of the model parameters in Table II was then chosen to give results for the polarizabilities midway between the extreme values. The cross sections were fitted using these parameters in order to obtain final results. The total model uncertainty was taken to be the combination-in-quadrature of the numbers in Table II. The results thus obtained are

$$\boxed{\bar{\alpha} - \bar{\beta} = 10.8 \pm 1.1 \pm 1.4 \pm 1.0} \quad (23)$$

and

$$\boxed{\bar{\alpha} + \bar{\beta} = 15.0 \pm 2.9 \pm 1.1 \pm 0.4} \quad (24)$$

where the errors are statistical, systematic, and model-dependent, respectively. As noted in Table II, if the individual contributions to the model-dependent errors are combined linearly rather than in quadrature, then the model-dependent errors on $\bar{\alpha} - \bar{\beta}$ and $\bar{\alpha} + \bar{\beta}$ become 2.0 and 0.7, respectively. Eqs. 23-24 represent the final results of the present experiment.

The result obtained for $\bar{\alpha} + \bar{\beta}$ agrees with the sum-rule value of $\bar{\alpha} + \bar{\beta} = 14.2 \pm 0.5$. Moreover, it was verified that the result obtained for $\bar{\alpha} - \bar{\beta}$ is independent of whether or not the sum-rule constraint is applied in the fit. The combination of Eq. 23 and the sum rule determines values for the individual polarizabilities:

$$\bar{\alpha} = 12.5 \pm 0.6 \pm 0.7 \pm 0.5 \quad (25)$$

$$\bar{\beta} = 1.7 \mp 0.6 \mp 0.7 \mp 0.5, \quad (26)$$

where the individual errors are anticorrelated due to the precise value of the sum.

C. Global Average

The present results were then compared with those of the previous experiments listed in Table I, and “global-average” values for $\bar{\alpha}$ and $\bar{\beta}$ were determined. As a first step, polarizabilities were extracted from each data set separately and compared to each other in order to check for overall consistency. The dispersion cross sections were used to fit to each of the data sets independently, without imposing the sum-rule constraint. The systematic errors were taken into account in the manner described above, with the only other free parameters being $\bar{\alpha} + \bar{\beta}$ and $\bar{\alpha} - \bar{\beta}$. Model parameters were chosen to reproduce approximately the average. In order to minimize the model dependence, the Saskatoon 1993

cross sections [10], all of which are above the pion threshold, were excluded from this analysis. The results are given in Table I and are shown in Fig. 10 in the form of error contours in the $\bar{\alpha}\bar{\beta}$ -plane, along with the constraint imposed by the dispersion sum rule, Eq. 2. It is evident that there is excellent overall consistency among all but the Moscow 1975 experiment [7]. As already mentioned, it was the inconsistency between that experiment and the sum rule that motivated the more recent experiments. The inconsistency can be traced to their 150° cross sections, which lead to a value of $\bar{\alpha} - \bar{\beta}$ that strongly disagrees with the other experiments. On the other hand, their 90° cross sections essentially determine $\bar{\alpha}$, which appears to be consistent with the other experiments. Nevertheless, in the determination of the global average, none of the Moscow 1975 data were considered.⁵

The dispersion cross sections were used to fit the remaining three data sets without the sum-rule constraint, taking into account the systematic errors and estimating the model uncertainty as described earlier. Global-average values for the polarizabilities are thus found:

$$\left(\bar{\alpha} - \bar{\beta}\right)_{\text{global}} = 10.0 \pm 1.5 \pm 0.9 \quad (27)$$

and

$$\left(\bar{\alpha} + \bar{\beta}\right)_{\text{global}} = 15.2 \pm 2.6 \pm 0.2, \quad (28)$$

where the first error is the combined statistical and systematic error propagated from the individual cross sections and the second is the model-dependent error derived in the manner described above. Once again, if the individual contributions to the model-dependent error are combined linearly, then the model-dependent errors approximately double. If instead the sum-rule constraint is applied to the global fit, the same value and error for $\bar{\alpha} - \bar{\beta}$ is found. The individual polarizabilities thus obtained are

$$\bar{\alpha}_{\text{global}} = 12.1 \pm 0.8 \pm 0.5 \quad (29)$$

⁵We note that including the 90° Moscow data in the global fit has essentially no effect on either the inferred value of $\bar{\alpha} - \bar{\beta}$ or its uncertainty.

and

$$\bar{\beta}_{\text{global}} = 2.1 \mp 0.8 \mp 0.5. \quad (30)$$

The error contour corresponding to the global fit with the sum-rule constraint is shown in Fig. 10.

VI. DISCUSSION

In recent years, various theoretical approaches have been used to calculate the polarizabilities of the nucleon, including non-relativistic quark models, bag models, chiral quark models, chiral perturbation theory, soliton models, and dispersion relations. An excellent review has been given by L'vov [33]. Here we elaborate on the dispersion-relation approach, which allows sum rules to be established for the polarizabilities. These sum rules are completely rigorous yet semi-phenomenological, since they relate the polarizabilities to features of the photoabsorption cross section. This is physically appealing, since it helps identify the physics that gives rise to $\bar{\alpha}$ and $\bar{\beta}$, such as the contribution of a particular nucleon resonance.

In the context of the fixed- t dispersion relations that were used to extract the polarizabilities from the Compton scattering data, two sum rules have already been presented: Eq. 21 for $\bar{\alpha} + \bar{\beta}$ and Eq. 19 for $\bar{\alpha} - \bar{\beta}$. It is illuminating to combine the two sum rules to obtain sum rules for $\bar{\alpha}$ and $\bar{\beta}$ separately, each of which can be written as a sum of an integral part and an asymptotic part:

$$\begin{aligned} \bar{\alpha} &= \bar{\alpha}^{\text{int}} + \bar{\alpha}^{\text{asympt}} \\ \bar{\beta} &= \bar{\beta}^{\text{int}} + \bar{\beta}^{\text{asympt}} \end{aligned} \quad (31)$$

The integral part can be directly evaluated using the single-pion multipole amplitudes and the model for the multi-pion multipole amplitudes. The asymptotic part is just the difference between the measured polarizability and the integral part. The values thus obtained are

$$\begin{aligned} \bar{\alpha}^{\text{int}} &\approx 5 & \bar{\alpha}^{\text{asympt}} &\approx 7 \\ \bar{\beta}^{\text{int}} &\approx 8 & \bar{\beta}^{\text{asympt}} &\approx -6 \end{aligned} \quad (32)$$

We first comment on the integral parts, the integrands for which are shown in Fig. 11. For $\bar{\alpha}^{\text{int}}$ the integral is dominated by multipoles involving non-resonant pion photoproduction, except for a negative contribution (~ -3) which comes from the excitation of the Δ resonance. Otherwise, there is apparently very little contribution from degrees of freedom associated with excitations of the valence quarks. Indeed, a qualitative calculation in the context of the chiral bag model [34] shows that both the electric polarizability and the diamagnetic part of the magnetic polarizability are dominated by the polarization of the pion cloud relative to the quark core and have little to do with the polarization of the core itself. This notion is confirmed by calculations using chiral perturbation theory at the one-loop order [35]. For $\bar{\beta}^{\text{int}}$ the integral is dominated by the Δ resonance [36].

We next comment on the asymptotic parts of the polarizabilities, which are neither small nor well constrained by the photoabsorption cross section. Indeed, the combination $\bar{\alpha} - \bar{\beta}$ is almost entirely due to the asymptotic contributions. As discussed in Section IV, these asymptotic contributions arise primarily from the t -channel exchange of a correlated pair of pions in a relative 0^+ state. In effect, it arises from the scattering from the pion cloud surrounding the nucleon. However, as pointed out by L'vov [33], the Born part of the scattering from the pion cloud is already largely contained in the integral contribution, so it is primarily the non-Born part that enters into the asymptotic amplitude. This idea receives support from an alternate sum-rule approach based on a backward dispersion relation [37]. There is a close correspondence between the asymptotic contribution to the fixed- t sum rule and the t -channel contribution to the backward sum rule, the latter involving the physical amplitudes for the process $\gamma\gamma \rightarrow \pi\pi \rightarrow N\bar{N}$. A substantial contribution to the t -channel integral is due to the non-Born part of $\gamma\gamma \rightarrow \pi\pi$, which is essentially due to pionic structure, including (but not limited to) the polarizability of the pion itself. This leads to the interesting possibility that a major contribution to the polarizability of the nucleon is due to the internal structure of the pions. Since the energy needed to excite the pion is large, this suggests that much of the physics of the nucleon polarizability is the physics of energies beyond 1 GeV. Any QCD-based structure model that attempts to calculate the polarizabilities will need to

address this physics.

VII. CONCLUSION

The Compton scattering cross section on the proton has been measured in the energy range 70–148 MeV, using both tagged and untagged photons. With the aid of fixed- t dispersion relations, new values for the electric and magnetic polarizabilities have been determined from these cross sections and the model-dependent uncertainty has been estimated. The present results have been combined with previously published Compton scattering cross sections below pion threshold in order to obtain global-average values for the polarizabilities. Dispersion relations indicate that the polarizabilities are only partially constrained by existing photoproduction data and that a substantial part is due to physics beyond 1 GeV, such as pionic structure.

ACKNOWLEDGMENTS

It is a pleasure to acknowledge many fruitful discussions with Dr. Anatoly L'vov and to thank him for providing us with his dispersion code. We gratefully acknowledge Prof. Dennis Skopik and the staff of the Saskatchewan Accelerator Laboratory for considerable technical and professional support during the setup and running of the experiment. We thank Mr. Erik Reuter for his work on the development of the gain monitoring system and Prof. Roy Holt for his helpful comments on this manuscript. This research was supported in part by the U. S. National Science Foundation under Grant Nos. NSF PHY 89-21146 and 93-10871 and by the Natural Sciences and Engineering Research Council of Canada.

APPENDIX: TABLES OF CROSS SECTIONS

The differential cross sections measured in the present experiment are tabulated in Tables III and IV. The correlations among the untagged cross sections required the fitting to

be done in a space where the error matrix is diagonal. The transformation of the original cross sections $\sigma_i = \sigma(E_i)$ (where $E_i = 105, 115, 125, 135, 145$ MeV) from the original space to the diagonal space σ'_j has the form

$$\sigma'_j = \sum_i V(j, i) \sigma(E_i). \quad (\text{A1})$$

This transformation is written explicitly for the 135° detector as:

$$\begin{aligned} \sigma'_1 &= +0.726 \sigma_1 - 0.575 \sigma_2 + 0.355 \sigma_3 - 0.123 \sigma_4 + 0.001 \sigma_5 \\ \sigma'_2 &= +0.121 \sigma_1 + 0.384 \sigma_2 + 0.603 \sigma_3 + 0.657 \sigma_4 + 0.205 \sigma_5 \\ \sigma'_3 &= -0.522 \sigma_1 - 0.245 \sigma_2 + 0.614 \sigma_3 - 0.165 \sigma_4 - 0.513 \sigma_5 \\ \sigma'_4 &= -0.334 \sigma_1 - 0.676 \sigma_2 - 0.211 \sigma_3 + 0.580 \sigma_4 + 0.224 \sigma_5 \\ \sigma'_5 &= -0.272 \sigma_1 - 0.065 \sigma_2 + 0.297 \sigma_3 - 0.435 \sigma_4 + 0.803 \sigma_5 \end{aligned}$$

and for the 90° detector as:

$$\begin{aligned} \sigma'_1 &= +0.206 \sigma_1 + 0.413 \sigma_2 + 0.711 \sigma_3 + 0.491 \sigma_4 + 0.203 \sigma_5 \\ \sigma'_2 &= -0.611 \sigma_1 + 0.748 \sigma_2 - 0.257 \sigma_3 + 0.013 \sigma_4 - 0.036 \sigma_5 \\ \sigma'_3 &= -0.613 \sigma_1 - 0.293 \sigma_2 + 0.625 \sigma_3 - 0.303 \sigma_4 - 0.236 \sigma_5 \\ \sigma'_4 &= -0.455 \sigma_1 - 0.426 \sigma_2 - 0.181 \sigma_3 + 0.646 \sigma_4 + 0.402 \sigma_5 \\ \sigma'_5 &= -0.029 \sigma_1 + 0.052 \sigma_2 + 0.078 \sigma_3 - 0.500 \sigma_4 + 0.860 \sigma_5. \end{aligned}$$

The fitting was done by transforming the calculated cross sections at the five energies 105, 115, 125, 135, 145 MeV into the new diagonal space, and fitting them to the uncorrelated cross sections in this space. The transformed cross sections and their uncorrelated errors (in units of nb/sr) for the 135° detector are:

$$\begin{aligned} \sigma'_1 &= 4.461 \pm 3.009 \\ \sigma'_2 &= 33.000 \pm 0.834 \\ \sigma'_3 &= -14.943 \pm 2.013 \\ \sigma'_4 &= -3.665 \pm 1.279 \\ \sigma'_5 &= 6.041 \pm 2.150 \end{aligned}$$

and for the 90° detector:

$$\sigma'_1 = 23.130 \pm 0.646$$

$$\sigma'_2 = 0.043 \pm 1.914$$

$$\sigma'_3 = -8.906 \pm 1.141$$

$$\sigma'_4 = 1.145 \pm 0.977$$

$$\sigma'_5 = 6.766 \pm 2.758.$$

REFERENCES

- * Present Address: Institute for Nuclear Study, University of Tokyo, Tokyo 188 Japan.
- † Present Address: Brookhaven National Laboratory, Upton, New York, 11973.
- [1] V. A. Petrun'kin, *Fiz. Elem. Chastits At. Yadra* **12** (1981) 692 [*Sov. J. Part. Nucl.* **12** (1981) 278].
- [2] J. L. Powell, *Phys. Rev.* **75**, 32 (1949).
- [3] A. M. Baldin, *Nucl. Phys.* **18**, 318 (1960); L. I. Lapidus, *Zh. Eksp. Teor. Fiz.* **43**, 1358 (1962) [*Sov. Phys. JETP* **16**, 964 (1963)].
- [4] M. Damashek and F. J. Gilman, *Phys. Rev. D* **1**, 1319 (1970).
- [5] A. I. L'vov, V. A. Petrun'kin, and S. A. Startsev, *Yad. Fiz.* **29**, 1265 (1979) [*Sov. J. Nucl. Phys.* **29**, 651 (1979)].
- [6] V. I. Gol'danski, *et al.*, *Zh. Eksp. Teor. Fiz.* **38**, 1695 (1960) [*Sov. Phys. JETP* **11**, 1223 (1960)].
- [7] P. S. Baranov, *et al.*, *Phys. Lett.* **52B** 122 (1974); P. S. Baranov, *et al.*, *Yad. Fiz.* **21**, 689 (1975) [*Sov. J. Nucl. Phys.* **21** (1975) 355]; P. S. Baranov, private communication.
- [8] F. J. Federspiel, *et al.*, *Phys. Rev. Letters*, **67**, 1511 (1991). See also F. J. Federspiel, Ph.D. dissertation, University of Illinois, 1991 (University Microfilms International)
- [9] A. Zieger, *et al.*, *Phys. Lett.* **B278**, 34 (1992).
- [10] E. L. Hallin, *et al.*, *Phys. Rev. C* **48**, 1497 (1993).
- [11] J. Bernabeu, *et al.*, *Phys. Lett.* **49B**, 381 (1974).
- [12] C. L. Oxley, *Phys. Rev.* **110**, 733 (1958).
- [13] B. E. MacGibbon, Ph.D. dissertation, University of Illinois, 1995 (University Microfilms International).

- [14] J. M. Vogt *et al.*, Nucl. Instr. and Meth. A **324**, 198 (1993).
- [15] J. H. Hubbell, Int. J. App. Radia. Isot. **33**, 1269 (1982).
- [16] W. R. Nelson, *et al.*, The EGS4 Code System (Version4), SLAC-265 (December 1985).
- [17] K. E. Mellendorf, Ph.D. dissertation, University of Illinois, 1993 (University Microfilms International).
- [18] L. I. Schiff, Phys. Rev. **83**, 252 (1951).
- [19] A. I. L'vov, Yad. Fiz. **34**, 1075 (1981) [Sov. J. Nucl. Phys. **34**, 597 (1981)], and private communication.
- [20] A. I. L'vov and A. M. Nathan, unpublished.
- [21] D. M. Akhmedov and L. V. Fil'kov, Yad. Fiz. **33**, 1083 (1981) [Sov. J. Nucl. Phys. **33**, 573 (1981)].
- [22] I. Guiaşu and E. E. Radescu, Phys. Rev. D **18**, 651 (1978).
- [23] W. J. Metcalf and R. L. Walker, Nucl. Phys. **B76**, 253 (1974).
- [24] R. A. Arndt, *et al.*, Phys. Rev. C **42**, 1853 (1990), and private communication. The tabulation of VPI multipole amplitudes may be obtained from the SAID program, which is available via TELNET at the site VTINTE.PHYS.VT.EDU.
- [25] Particle Data Group, Phys. Rev. D **50**, 1173 (1994).
- [26] V. Stoks, *et al.*, Phys. Rev. C **47**, 512 (1993).
- [27] J. Duda, *et al.*, Z. Phys. C **17**, 319 (1983).
- [28] E. L. Berger, *et al.*, Phys. Rev. D **17**, 2971 (1978).
- [29] M. M. Nagels, *et al.*, Phys. Rev. D **12**, 744 (1975).
- [30] T. A. Armstrong, *et al.*, Phys. Rev. D **5**, 1640 (1972).

- [31] H. Rollnik and P. Stichel, *Springer Tracts in Modern Physics, Vol. 79* (Springer-Verlag, Berlin, 1976), p. 39.
- [32] G. D'Agostini, Nucl. Instr. Meth. **A346**, 306 (1994).
- [33] A. I. L'vov, Int. J. Mod. Phys A **8**, 5267 (1993).
- [34] R. Weiner and W. Weise, Phys. Lett. **159B**, 85 (1985).
- [35] V. Bernard, *et al.*, Z. Phys. A **348**, 317 (1994); Phys. Lett. B **319**, 269 (1993).
- [36] N. Mukhopadhyay, *et al.*, Phys. Rev D **47**, R7 (1993).
- [37] B. R. Holstein and A. M. Nathan, Phys. Rev. D **49**, 6101 (1994).

TABLES

TABLE I. Measurements of the proton polarizabilities in units of 10^{-4} fm^3 . The values and errors are not from the original publications but were derived by us from the published cross sections using the techniques described in Section V. The first error is the combined statistical and sytematic error, and the second is an estimate of the uncertainty due to the model.

Data Set	Energies (MeV)	Angles	$\bar{\alpha} + \bar{\beta}$	$\bar{\alpha} - \bar{\beta}$
Moscow 1975 [7]	70–110	$90^\circ, 150^\circ$	$5.8 \pm 3.3 \pm 0.2$	$17.8 \pm 2.0 \pm 0.9$
Illinois 1991 [8]	32–72	$60^\circ, 135^\circ$	$15.8 \pm 4.5 \pm 0.1$	$11.9 \pm 5.3 \pm 0.2$
Mainz 1992 [9]	98, 132	180°	— — — — —	$7.6 \pm 2.9 \pm 1.0$
Saskatoon 1993 [10]	149–286	24° – 135°	$12.1 \pm 1.7 \pm 0.9$	$7.9 \pm 1.4 \pm 2.0$
present work	70–148	$90^\circ, 135^\circ$	$15.0 \pm 3.1 \pm 0.4$	$10.8 \pm 1.8 \pm 1.0$

TABLE II. Sensitivity of the extracted values of $\bar{\alpha} + \bar{\beta}$ and $\bar{\alpha} - \bar{\beta}$ to model-dependent uncertainties in the dispersion calculations. The numbers in columns 2 and 3 are the spread in values obtained from the present experiment (in units of 10^{-4} fm^3) when the parameters in column 1 are changed within the range shown or discussed in the text. The last two rows show the results of combining these spreads in quadrature and linearly.

Model Parameter	$\Delta(\bar{\alpha} + \bar{\beta})$	$\Delta(\bar{\alpha} - \bar{\beta})$
Single-pion multipoles	± 0.15	± 0.25
Multi-pion multipoles	± 0.25	± 0.15
π^0 -exchange coupling ($\pm 4\%$)	± 0.00	± 0.30
B_π (0–3 GeV^{-2})	± 0.00	± 0.65
$B_{2\pi}$ (6–10 GeV^{-2})	± 0.25	± 0.60
B_P (6–10 GeV^{-2})	± 0.00	± 0.00
combined in quadrature	± 0.38	± 0.98
combined linearly	± 0.65	± 1.95

TABLE III. Tagged differential cross sections for each angle and the statistical error.

Central Photon Energy (MeV)	$\frac{d\sigma}{d\Omega}(135^\circ)$ (nb/sr)	$\frac{d\sigma}{d\Omega}(90^\circ)$ (nb/sr)
73.2	14.33 ± 1.81	10.41 ± 1.66
81.8	16.06 ± 1.77	8.97 ± 1.60
89.8	16.71 ± 1.68	10.72 ± 1.49
96.8	16.05 ± 1.63	8.61 ± 1.40

TABLE IV. Untagged differential cross sections for each angle along with the corresponding diagonal terms in the error matrix.

Energy Range (MeV)	$\frac{d\sigma}{d\Omega}(135^\circ)$ (nb/sr)	$\frac{d\sigma}{d\Omega}(90^\circ)$ (nb/sr)
100–110	14.60 ± 2.53	9.48 ± 1.44
110–120	15.87 ± 2.03	12.07 ± 1.56
120–130	14.88 ± 1.84	11.19 ± 1.02
130–140	18.85 ± 1.40	11.40 ± 1.59
140–150	18.45 ± 2.04	13.07 ± 2.42

FIGURES

FIG. 1. Calculations of the Compton scattering cross section from the proton, showing the cross section for the point proton (Born), the LEX, and the fixed- t dispersion relations (DR). The calculations assume that $\bar{\alpha} + \bar{\beta} = 14.2$ and $\bar{\alpha} - \bar{\beta} = 9.0$.

FIG. 2. A schematic of the photon scattering techniques used in this experiment, showing the calibration measurement (upper half) and the scattering measurement (lower half). Sample tagged and untagged photon spectra were generated by a Monte Carlo simulation.

FIG. 3. Tagged photon calibration spectrum and Monte Carlo fit.

FIG. 4. TDC spectra for the 135° detector, summed over all channels of the tagger. The TDC is started by a photon signal from the NaI and stopped by an electron signal from the tagger focal plane. Each TDC channel corresponds to 0.1 ns. The cuts applied for the true and random coincidences are indicated.

FIG. 5. Tagged spectrum of photons scattered from hydrogen at 135° and Monte Carlo fit.

FIG. 6. Untagged photon calibration spectrum and Monte Carlo fit.

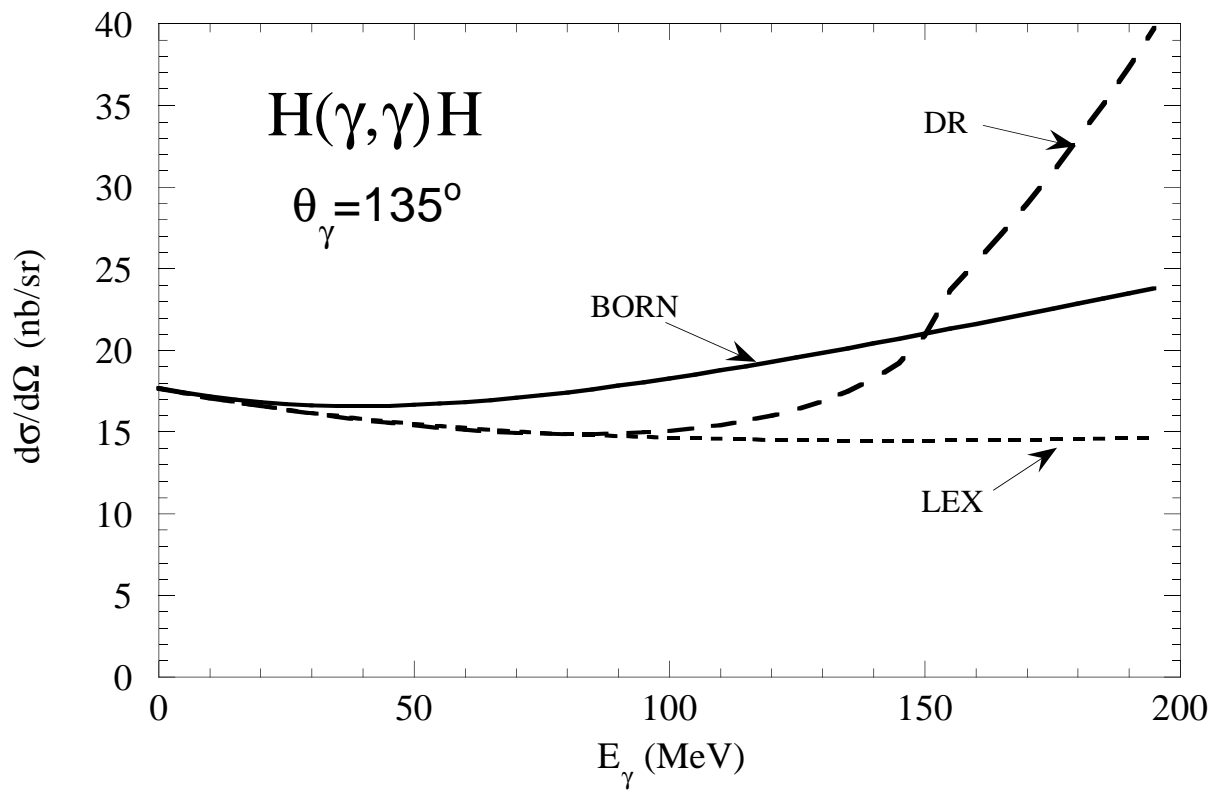
FIG. 7. Untagged spectra of photons scattered from hydrogen at 90° and 135° and Monte Carlo fits. Using the tagged cross sections, the calculation has been extended into the tagging region, which is to the left of the vertical line.

FIG. 8. Diagrams for Compton scattering from the proton, including s -channel and u -channel processes as well as t -channel exchanges.

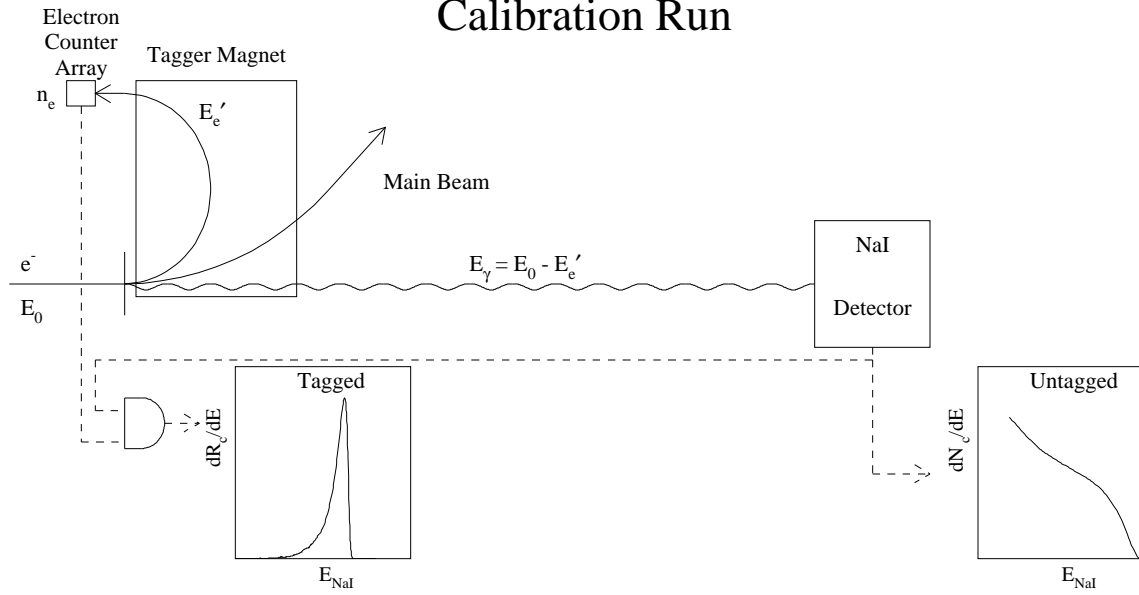
FIG. 9. Cross sections measured in the present experiment (open circles) and curves calculated with the fixed- t dispersion relations using $\bar{\alpha} + \bar{\beta}=14.2$, $\bar{\alpha} - \bar{\beta}=10.8$, and a particular set of model parameters. Also shown are the data of Goldansky (closed triangles) [6], Baranov (open squares) [7], Federspiel (closed squares) [8], and Hallin (open triangles) [10].

FIG. 10. Error contours in the $\bar{\alpha}\bar{\beta}$ -plane for the experiments listed in Table I and for the dispersion sum rule. Also shown is the error contour for a global fit to all the data, excluding the Moscow 1975 cross sections, as described in the text. The contours correspond to one standard deviation for the combined statistical and systematic errors, and the values are for one set of model parameters.

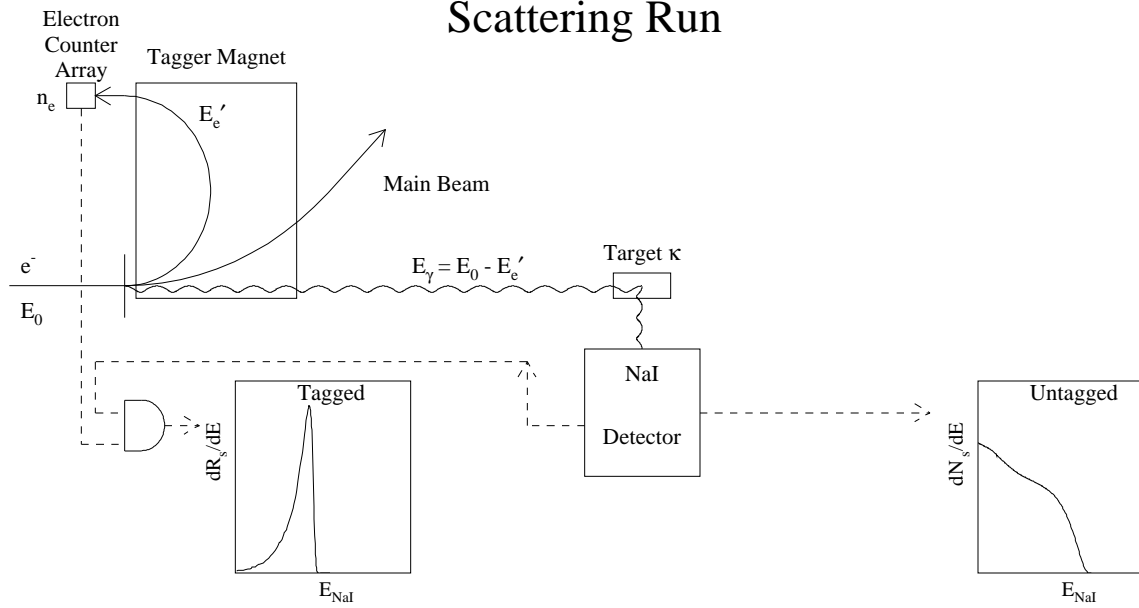
FIG. 11. Integrands for $\bar{\alpha}^{\text{int}}$ (solid curve) and $\bar{\beta}^{\text{int}}$ (dashed curve).

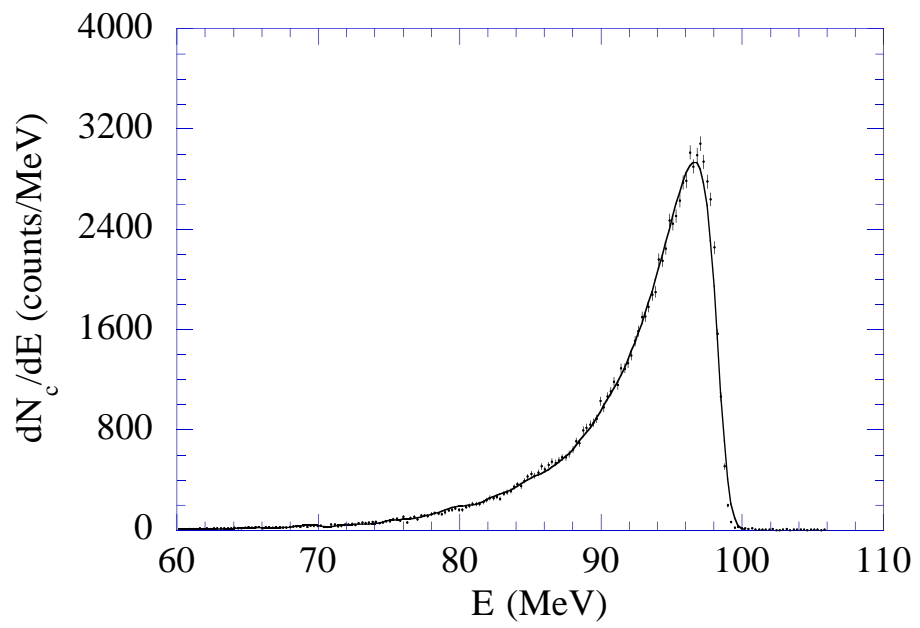


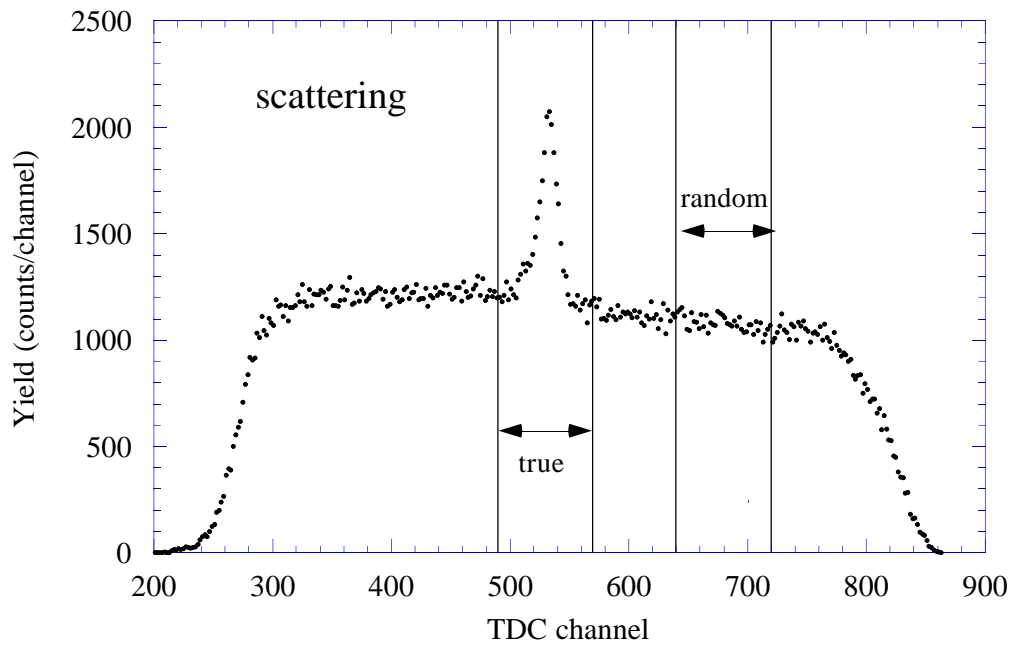
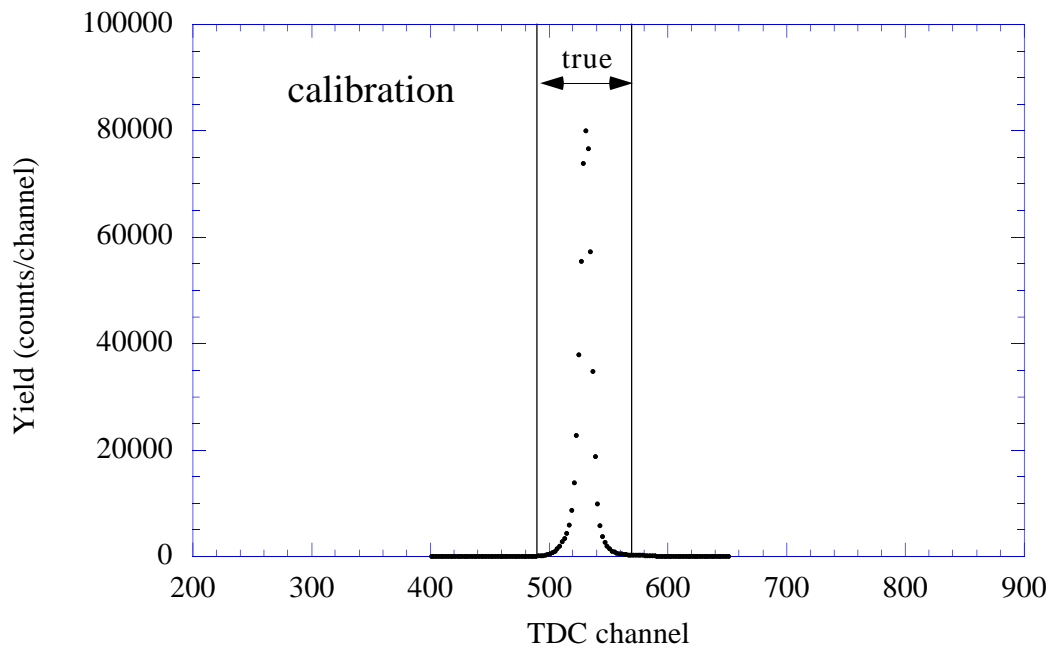
Calibration Run

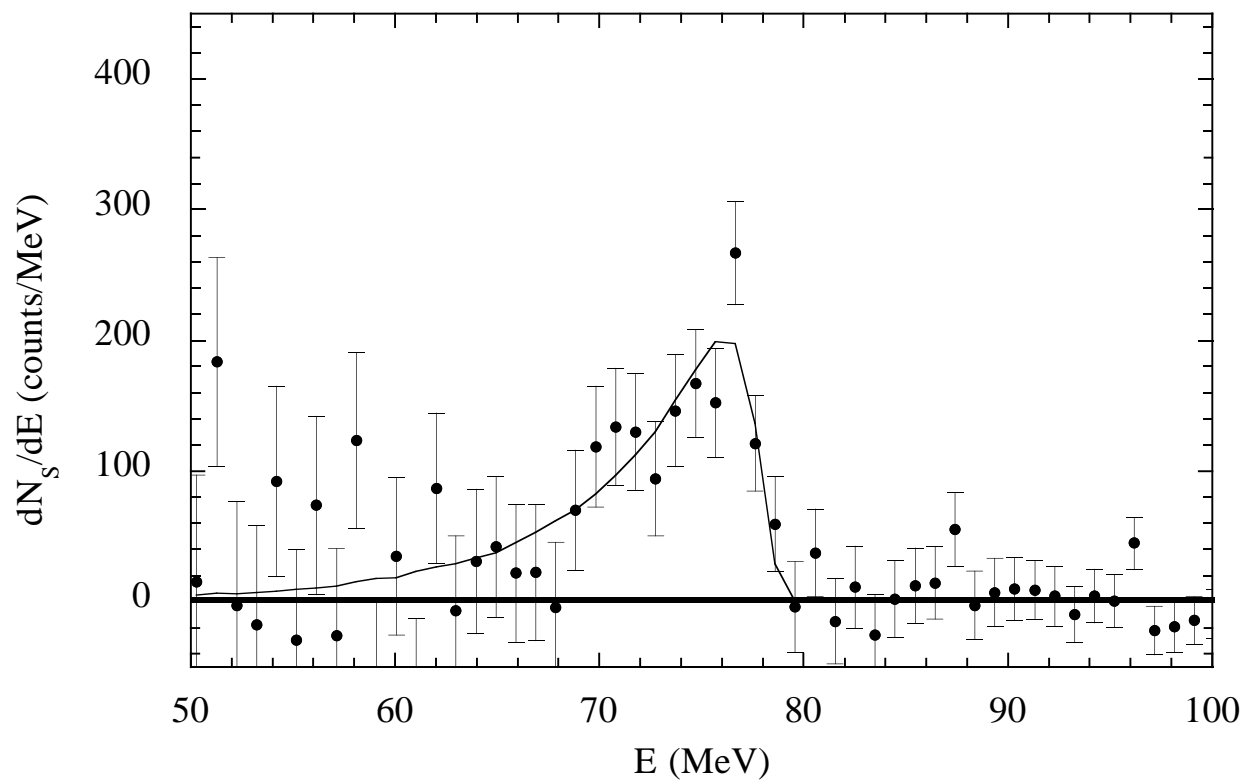


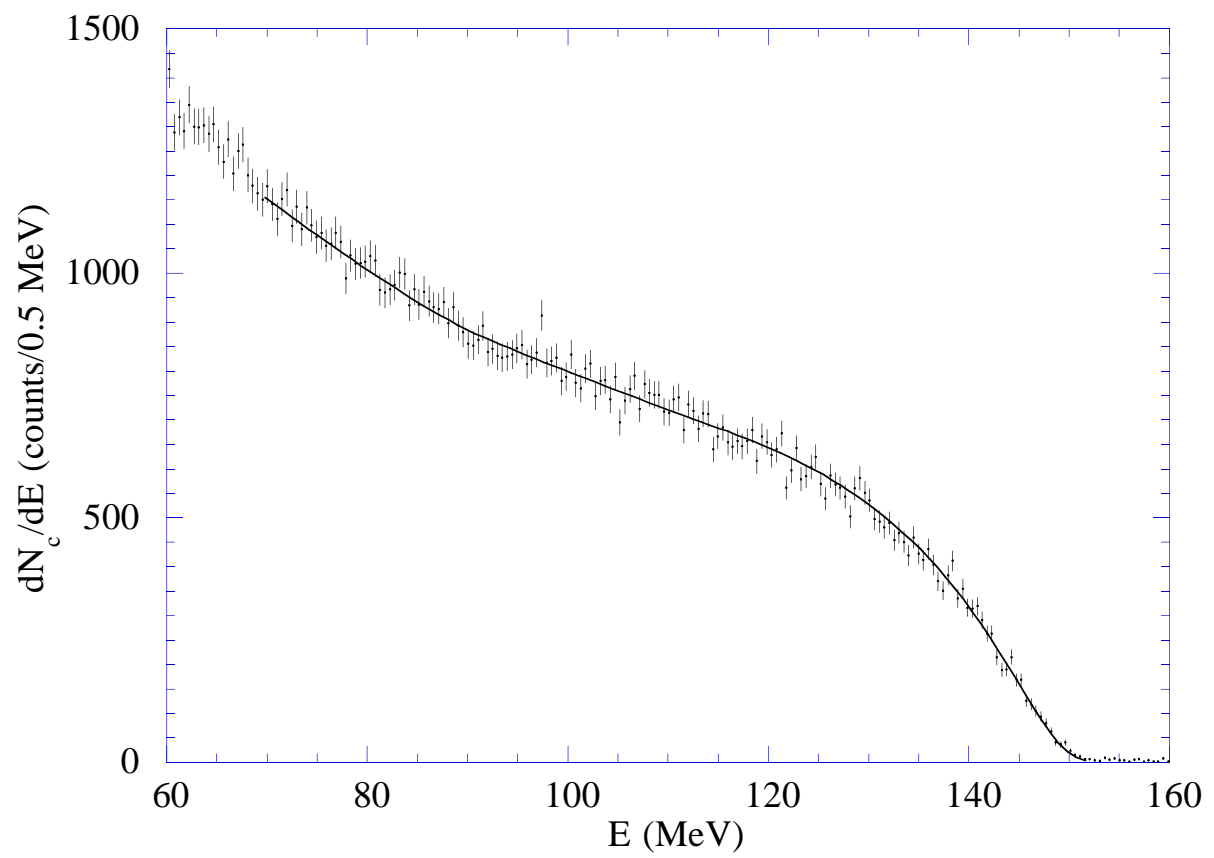
Scattering Run

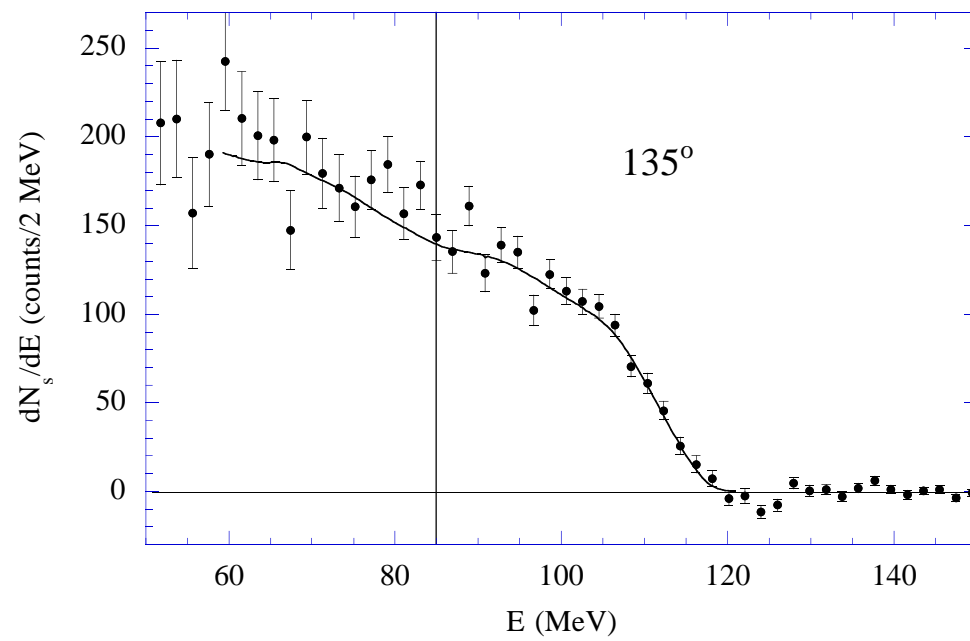
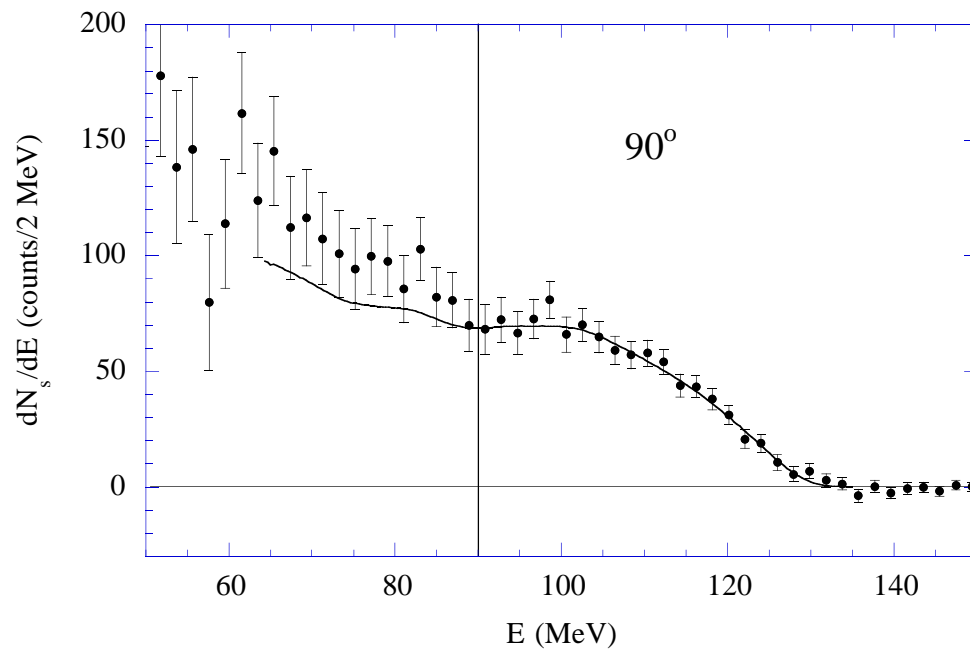


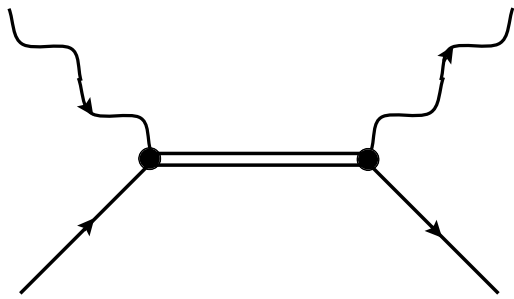




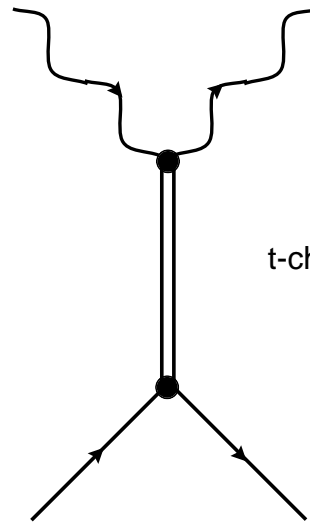




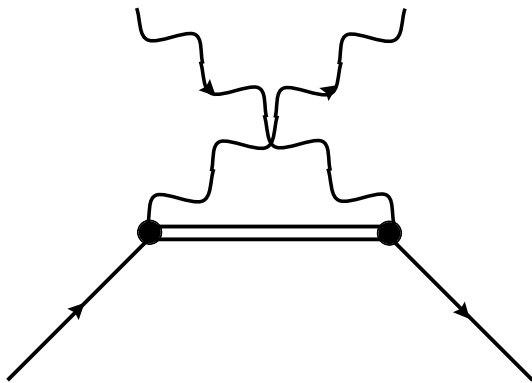




s-channel



t-channel



u-channel

